Dynamic Nanocatalysis
https://www.sciltp.com/journals/dn

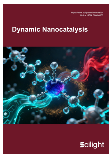

Article

Unraveling the Mechanism and Activity of a Spherical Fe_2O_3-$CoFe_2O_4$ Mixed Oxide Catalyst in NH_3-SCR of NO_x

Bingyi Xin, Ting Zhu, Hui Wang * and Zhenping Qu

Key Laboratory of Industrial Ecology and Environmental Engineering (MOE), School of Environmental Science and Technology, Dalian University of Technology, No. 2 Linggong Road, Dalian 116024, China
* Correspondence: wanghui2017@dlut.edu.cn

How To Cite: Xin, B.; Zhu, T.; Wang, H.; et al. Unraveling the Mechanism and Activity of a Spherical Fe_2O_3-$CoFe_2O_4$ Mixed Oxide Catalyst in NH_3-SCR of NO_x. *Dynamic Nanocatalysis* **2026**, *1*(1), 3. https://doi.org/10.53941/dn.2026.100003

Received: 3 April 2026
Revised: 3 May 2026
Accepted: 6 May 2026
Published: 11 May 2026

Abstract: A spherical spinel catalyst system based on $CoFe_2O_4$ was successfully fabricated, and the influence of the spinel and composite structure on the catalytic activity and physicochemical properties of the catalyst were systematically investigated. The Fe_2O_3-$CoFe_2O_4$ spherical spinel composite catalyst demonstrated significantly improved NH_3-SCR performance achieving ≥ 80% NO_x conversion in the temperature range of 225–300 °C. Its NO_x conversion was 3.03 times that of Fe_2O_3 and 7.45 times that of Co_3O_4 at 225 °C. This enhancement is attributed to the synergistic interaction between the Fe_2O_3 and $CoFe_2O_4$. In the inverse spinel structure of $CoFe_2O_4$, Fe^{3+} occupy both tetrahedral and octahedral sites, which facilitates NH_3 and NO_x adsorption. Meanwhile, the electronic interaction between Fe_2O_3 and $CoFe_2O_4$ leads to a corresponding decrease in the electron cloud density of Co, thereby enhancing their electrophilicity and further promoting the adsorption and stabilization of NO_3^- species. Furthermore, in situ DRIFTS results showed that coordinated NH_3 and nitrate species served as the dominant reactive intermediates, following the Langmuir-Hinshelwood pathway. The reaction between bidentate nitrates and adsorbed NH_3 was identified as the rate-determining step.

Keywords: $CoFe_2O_4$; spherical; Fe_2O_3; NH_3-SCR; NO_x

1. Introduction

The increasing global concern over air quality has placed stringent regulations on the emission of nitrogen oxides (NO_x, $x = 1, 2$), which are primarily generated from industrial combustion processes, including power generation, steel manufacturing, and transportation. NO_x not only causes environmental issues such as acid rain and ground-level ozone formation but also poses significant risks to human health. Among the available control technologies, selective catalytic reduction NO_x with NH_3 (NH_3-SCR) is considered the most effective and established method for NO_x removal [1,2]. The pursuit of advanced catalysts with superior activity, broad temperature windows, and robust durability remains a key research priority.

Spinel metal oxides, with the general formula AB_2O_4, have attracted considerable attention in the field of heterogeneous catalysis due to their tunable electronic structures, diverse atomic compositions, and flexible physicochemical properties. In the AB_2O_4 structure, A is in the tetrahedral position of AB_2O_4, while B is in the octahedral position. The lattices of tetrahedral and octahedral positions can be replaced by different types of cations, and the cations between A and B sites can migrate to each other, forming A surface rich in oxygen vacancy. These characteristics are conducive to the regulation of AB_2O’s acid-base position and REDOX properties, thus promoting the catalytic activity of NH_3-SCR [3,4]. Generally, the metal oxides of spinel can be divided into normal spinel and anti-spinel according to the different crystal structure [5]. In its cellular structure, metal ions at A and B positions occupy tetrahedral and octahedral elements surrounded by oxygen atoms, respectively. Generally, the octahedral space is larger than the tetrahedral space, so the metal ions with A small radius tend to occupy the A site, while the metal ions with A large radius tend to occupy the B site. In the structural formula of normal spinel, A and B are metal cations with +2 valence and +3 valence respectively, while the anti-spinel structure is mainly described in the form of $B(AB)O_4$, in which the metal cations with +2 valence are filled into the space of octahedral body position, and half of the +3 valence metal cations are filled into the space of tetrahedron.

In trans spinel structure, eight surface position occupied state can be orderly state or random state, and the random state of metal cations occupying state leads to defect of the spinel structure is among the more typical MFe_2O_4 ferrite materials, different site of M^{2+} ion composition can lead to material performance differences, so changing the atoms in spinel metal oxide can regulate the chemical and physical properties of catalyst, then improving the catalytic performance [6]. $CoFe_2O_4$ is a typical inverse spinel, which can be expressed as $(Fe^{3+})_{tet}$ $(Co^{2+}\ Fe^{3+})_{oct}O_4$ [4,7]. Owing to the weak tendency of Fe^{3+} ions to occupy either A or B sites in iron spinels, the distribution of doped ions between A and B sites becomes indeterminate, thereby correspondingly facilitating the diversity of ionic valence states and the formation of oxygen vacancies.

At the same time, the structure and morphology regulation of the catalyst is also a method to improve the catalytic performance. The morphology and structural characteristics of catalysts are important factors affecting their application. For example, materials containing multi-layer hollow nanostructures have many excellent physical and chemical properties, such as large specific surface area, low density and a large number of active sites. R. A. Kadam et al. [8] found that hierarchical $ZnFe_2O_4$ flower-like nanostructures exhibit significantly enhanced light absorption, enlarged specific surface area, and improved charge carrier dynamics compared to aggregated nanoparticles. K. Lazaar et al. [9] fabricated sea urchin-like $NiCo_2O_4$ microspheres with favorable photocatalytic activity through a precisely controlled hydrothermal route, with the reaction conducted at 180 °C for durations ranging from 6 to 16 h. L. C. C. Arzuza et al. [10] successfully prepared high-quality CFO nanofibers featuring a porous surface morphology. Electrocatalytically, CFO nanofibers calcined at 500 °C showed a low overpotential of 313 mV (vs. RHE) at 10 mA cm^{-2} and a high TOF of 0.016 s^{-1} at 500 mV, ranking among top-performing CFO-based catalysts reported.

Recent advances in spinel-based catalysts have further underscored their potential for NH_3-SCR applications. Zheng et al. [11] constructed a hierarchically porous spinel $CoMn_2O_4$ via a ZIF-derived strategy, achieving over 90% NO_x conversion at 150 °C by facilitating the fast SCR pathway through enriched oxygen vacancies and surface acid sites. Similarly, Hou et al. [12] demonstrated that the rational design of acidic and redox sites in Mn-based spinels significantly enhances low-temperature SCR activity. Zhao et al. [13] combined DFT calculations with in situ DRIFTS to elucidate the reaction mechanism of NH_3-SCR over $CrMn_2O_4$ spinel, confirming that electrophilic Mn atoms play a central role in reactant activation. Despite these significant advances, studies that simultaneously achieve controlled spherical morphology, resolve the interfacial electronic synergy between composite phases, and identify the molecular-level reaction pathway remain scarce.

In this work, a spherical core-shell Fe_2O_3-$CoFe_2O_4$ catalyst was constructed by simply tuning the hydrothermal duration. This approach enabled precise control over phase composition and interfacial contact, revealed a synergistic electronic interaction that enhances NH_3 and NO_x adsorption/activation, and identified the dominant surface intermediates and reaction pathway via in situ DRIFTS. Consequently, a clear structure-property-performance relationship is established for this catalyst in NH_3-SCR, providing a straightforward strategy for designing advanced mixed-oxide catalysts.

2. Experimental

2.1. Catalyst Preparation

Spherical Co-Fe (6 and 8 h) were synthesized by a hydrothermal method. All reagents were analytical grade and used as received without further purification. $Fe(NO_3)_3\cdot 9H_2O$ and $Co(NO_3)_2\cdot 6H_2O$ were used as salt precursors, the mixture of glycerol and isopropanol as solvent. Typically, 0.25 mmol $Co(NO_3)_2\cdot 6H_2O$ was added into 70 mL isopropanol and mixed uniformity, then 14 mL glycerol was added followed 0.5 mmol $Fe(NO_3)_3\cdot 9H_2O$ was added into mixture under constant stirring. After becoming homogeneous solution, the mixture was transferred into a 100 mL sealed Teflon-lined autoclave. Next, the mixture was placed in an oven of 180 °C for 6 and 8 h followed by filtration, washing with ethanol and dried at 60 °C to obtain Co-Fe glycerate precursors (denoted as Co-Fe(gp)). Finally, the as-synthesized Co-Fe(gp) was calcined under 500 °C for 2 h at a rate of 1 °C/min. The designed Co-Fe complex oxides synthesized at the hydrothermal time of 6 and 8 h are denoted as Co-Fe (6 h) and Co-Fe (8 h), respectively. For comparison, pure Fe_2O_3 and Co_3O_4 samples were also prepared by hydrothermal method. Subsequently, the catalysts were crushed and sieved to a particle size of 20–40 mesh prior to activity evaluation. Each sample was prepared in triplicate to ensure reproducibility of the preparation method.

2.2. Activity Measurement

Catalytic performance was evaluated by using a fixed-bed quartz tubular reactor. Reaction conditions as follows: 500 ppm of NH_3, 500 ppm of NO, 3 vol. % O_2, N_2 balance and 300 mL/min total flow rate. The catalyst used for activity test with a gas hourly space velocity (GHSV) of 60,000 h^{-1}. The concentration of NO_x in the inlet and outlet gases was detected by a NO-NO_2-NO_x Analyzer (42i-HL, Thermo Scientific).

Using following equations to calculate the NO_x conversion (%):

$$NO_x \text{ conversion}(\%) = \frac{[NO_x]_{in} - [NO_x]_{out}}{[NO_x]_{in}} \times 100\%$$

where $[NO_x]_{in}$ and $[NO_x]_{out}$ (x = 1, 2) represented the inlet and outlet NO_x concentrations in the feed gas, respectively.

2.3. Catalyst Characterization

X-ray diffraction (XRD) patterns of the samples were recorded on a Rigaku D/MAX-2500 X-ray diffractometer with copper Kα radiation (λ = 1.54 Å) in the range from 10° to 90° with 5°/min. The morphologies and microstructure information of the catalysts are obtained by a transmission electron microscope (TEM) images of the catalysts were obtained using Tecnai F30 electron microscope equipped with a field emission source operating at 300 kV.

X-ray photoelectron spectroscopy (XPS) was performed by K-Alpha+ instrument equipped with the analysis room vacuum is 5×10^{-9} mbar, multifunctional imaging electron spectrometer using a monochromatic Al Kα radiation, and the binding energies of Fe 2*p*, Co 2*p*, and O 1*s* were calibrated using the C 1*s* peak (BE = 284.8 eV) as standard. Temperature-programmed reduction by hydrogen (H_2-TPR) was carried out on a Quantachrom automated chemisorption analyzer with 100 mg of each catalyst. Prior to each test, the catalyst was pretreated in a flowing N_2 (20 mL/min) at 200 °C for 30 min and then cooled to room temperature in a N_2 flow. By switching to 10 vol. % H_2, TPR experiment was carried out in the range of 30–800 °C with a ramping rate of 10 °C/min and monitored online by TCD detector.

Temperature-programmed desorption of NH_3 (NH_3-TPD) was implemented on the same instrument with 100 mg of sample. After pretreatment (50 mL/min He flow, 200 °C for 30 min) and then the sample was cooled down to room temperature. Subsequently, adsorption of 500 ppm NH_3/He at room temperature for 30 min to ensure the sufficient adsorption of NH_3. Before desorption, the sample was purged by a flowing He stream at same temperature for 90 min to remove excessive and physically adsorbed NH_3. Finally, the sample was heated from 30 to 730 °C at a rate of 10 °C/min in a pure He (50 mL/min) flow and desorption pattern was recorded in a fixed-bed flow reactor with a computer-interfaced quadruple mass spectrometer (MS, Pfeiffer OmniStar) as detector. Temperature-programmed desorption of NO + O_2 (NO + O_2-TPD) was tested same with temperature-programmed desorption of NH_3 (NH_3-TPD), except replacing NH_3 with NO + O_2.

The in situ diffusion Fourier transform infrared spectroscopy (in situ DRIFTS) experiments were performed on a Bruker VERTEX 70 FTIR spectrometer equipped with a highly-sensitive MCT detector cooled with liquid nitrogen. Prior to each experiment, the sample was pretreated in a He flow at 300 °C for 1 h to remove adsorbed impurities and cooled to the desired temperature, a background spectrum was collected under a flowing He atmosphere and was subtracted from the sample spectra from 800 to 4000 cm^{-1} with a spectral resolution of 4 cm^{-1}. For each process, the total flow rate was kept at 100 mL/min with the following reaction gases: 500 ppm of NH_3, 500 ppm of NO, 3 vol. % O_2, and He as balance. The DRIFT spectra were recorded by accumulating 32 scans with a resolution of 4 cm^{-1}.

3. Results and Discussion

3.1. Confirmation of Catalyst Species

In order to determine the phases and chemical compositions of prepared Co-Fe serials catalysts, the XRD detection was carried out accordingly. The XRD patterns of Co-Fe (6 and 8 h), pure Fe_2O_3 and Co_3O_4 are shown in Figure 1a. The results display the pristine Fe_2O_3 and Co_3O_4 are in the typical hematite and cubic phase, respectively, with sharp and intense diffraction peaks indicating their highly crystalline nature. The diffraction peaks of the sample prepared with a hydrothermal time of 6 h are consistent with the standard spectra of $CoFe_2O_4$ spinel (JCPDS:22-1086). But for Co-Fe (8 h) catalyst, some diffraction peaks of α-Fe_2O_3 are detected besides the diffraction peaks of $CoFe_2O_4$ spinel, which indicates that the Co-Fe (8 h) catalyst is composed of $CoFe_2O_4$ and α-Fe_2O_3. The TEM images (Figure 1b,c) show that the Co-Fe catalysts synthesized with hydrothermal treatment times of 6 h and 8 h both display a relatively uniform spherical core-shell structure, with diameters of approximately 500 nm. Measurements indicate a shell thickness of about 25 nm and a core size of roughly 400 nm. Figure 1d shows the EDS mapping results of the Co-Fe (8 h) catalyst. The signals of Fe, Co, and O exhibit a discrete punctate distribution across the entire field of view, with high-intensity regions highly coincident with the dark areas in the transmission image, indicating that Fe, Co, and O elements are enriched at specific lattice sites. This confirms the successful synthesis of spherical Co-Fe complex oxides. The above results demonstrate that $CoFe_2O_4$ and Fe_2O_3-$CoFe_2O_4$ spherical spinel were successfully synthesized by varying the hydrothermal time.

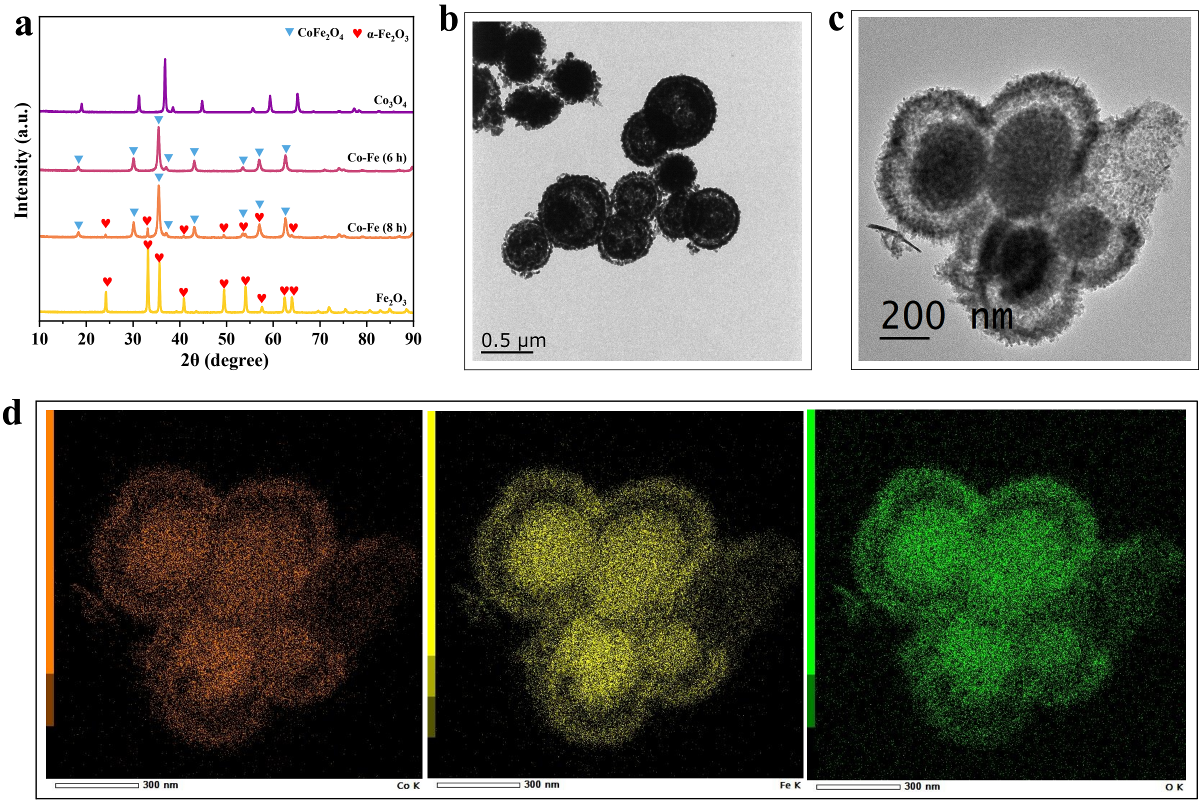

Figure 1. The structure of the prepared catalysts: (**a**), XRD patterns; (**b**,**c**) TEM micrographs result of Co-Fe (6 h) and Co-Fe (8 h), respectively; (**d**) mapping result of Co-Fe (8 h) catalyst.

3.2. Chemical Properties Analysis

The information on the surface electronic states and redox properties in the Co-Fe mixed oxides serial catalysts could be obtained from XPS and H_2-TPR technique.

The XPS spectra of Fe 2*p*, Co 2*p* and O 1*s* are shown in Figure 2a–c. The pristine Co_3O_4 exhibits Co 2*p* binding energies at 778.1 eV and 794.3 eV, along with a satellite peak at 789.8 eV, which are consistent with those of standard Co_3O_4 [14,15]. Notably, the satellite peak of the Co-Fe sample appears at a lower binding energy and is more obvious compared with that of Co_3O_4, which is characteristic of Co^{2+} species [16,17] and further confirms the formation of inverse spinel $CoFe_2O_4$ ($(Fe^{3+})_{tet}$ $(Co^{2+}\ Fe^{3+})_{oct}O_4$). Furthermore, compared with the Co-Fe (6 h) sample, the Co 2*p* peaks of the Co-Fe (8 h) sample shift to lower binding energy, indicating a stronger electron interaction between the $CoFe_2O_4$ and Fe_2O_3 species. This interaction results in the significant binding energy deviation and a corresponding decrease in density of the electron cloud of Co. The pristine Fe_2O_3 catalyst has the highest binding energies at 710.6 eV and 724.0 eV (Figure 2b), which accorded well with Fe $2p_{3/2}$ and Fe $2p_{1/2}$, respectively, indicating that the Fe species in the catalyst are mainly Fe^{3+} [18–20]. For the Co-Fe (6 h) and Co-Fe (8 h) samples, two well-defined peaks are observed at 710.6 eV (Fe $2p_{3/2}$) and 723.8 eV (Fe $2p_{1/2}$), suggesting that the valence state of Fe remains unchanged. Meanwhile, the O 1*s* spectra of Co-Fe catalysts (Figure 2c) are fitted into two peaks corresponding to the lattice oxygen O^{2-} (O_β) (529.52–531.01 eV) and surface adsorbed oxygen species (O_α) (530.55–532.38 eV) [18,21]. The peak area can be used to calculate $O_\alpha/(O_\alpha + O_\beta)$. The $O_\alpha/(O_\alpha + O_\beta)$ value of the Co-Fe (6 h) catalyst is 28.2%, whereas that of the Co-Fe(8 h) catalyst decreases to 22.7%. Notably, the $O_\alpha/(O_\alpha + O_\beta)$ ratio of Co-Fe(8 h) decreased to, indicating that the strong interaction between $CoFe_2O_4$ and Fe_2O_3 is detrimental to the formation of oxygen vacancies.

The H_2-TPR profiles are illustrated in Figure 2d. For Fe_2O_3, the reduction peaks at 393, 633, 784 °C could be attributed to the reduction of $Fe_2O_3 \rightarrow Fe_3O_4$, $Fe_3O_4 \rightarrow FeO$ and $FeO \rightarrow Fe$, respectively [22,23]. The Co_3O_4

catalyst exhibits two overlapped reduction peaks at 300~400 °C, which are ascribed to the reduction of $Co^{3+} \rightarrow Co^{2+}$ and $Co^{2+} \rightarrow Co$, respectively [24,25]. In contrast, the Co-Fe (6 and 8 h) exhibit markedly different reduction behavior. Compared with pure Co_3O_4, the reduction temperatures shift to higher values, which is consistent with the presence of Co^{2+} in the $CoFe_2O_4$ spinel structure. Notably, the Co-Fe (8 h) catalyst exhibits a higher reduction temperature than the Co-Fe (6 h) sample, which is ascribed to the enhanced electron interaction between Fe_2O_3 and $CoFe_2O_4$ resulting from the more intimate interfacial contact in the composite.

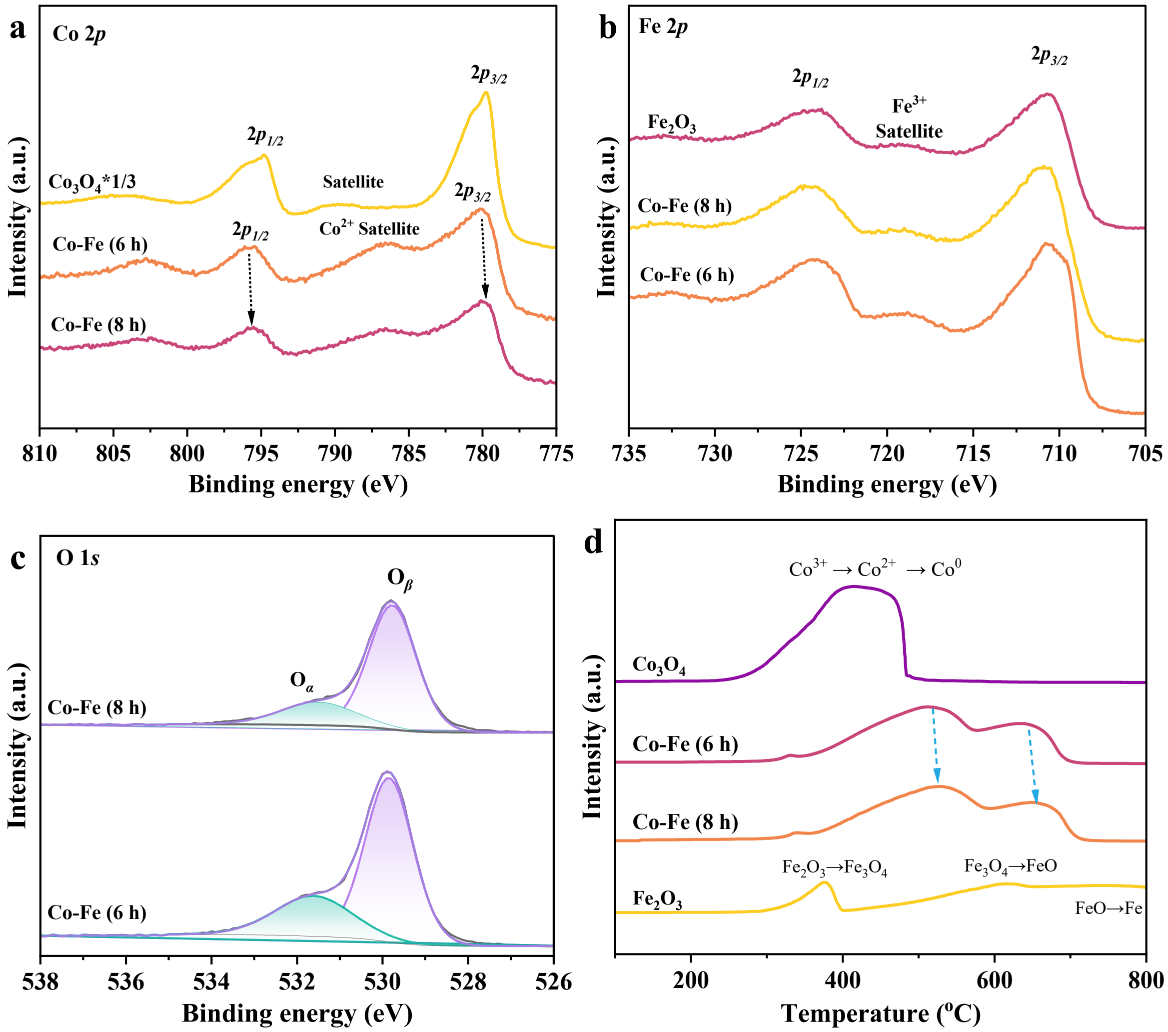

Figure 2. The chemical properties of the prepared catalysts: (**a**–**c**) XPS spectra; (**d**) H_2-TPR profiles.

3.3. Catalytic Performances

The NH_3-SCR performance of the catalysts is shown in Figure 3a. Pristine Fe_2O_3 and Co_3O_4 exhibits poor activity, with a maximum NO_x conversion of only 41.4% at 275 °C and 24.3% at 300 °C, respectively. In contrast, the Co-Fe (6 h) sample, which consists of the inverse spinel $CoFe_2O_4$, shows significantly enhanced activity, achieving over 80% NO_x conversion in the range of 225–300 °C, with a peak of 85.5%. This confirms that the inverse spinel $CoFe_2O_4$ is a more active species than normal spinel Co_3O_4. Notably, further prolonging the hydrothermal time to 8 h (Co-Fe (8 h)) leads to a further improvement, expanding the operation window to 225–325 °C and increasing the maximum conversion to 92.4%. The superior activity of Co-Fe (8 h) is attributed to the synergistic interaction between the Fe_2O_3 and $CoFe_2O_4$ spinel phases, which further promotes SCR activity and broadens the effective temperature window.

To further investigate the catalyst's resistance to high gas hourly space velocities (GHSV), the Co-Fe (8 h) catalyst was tested under GHSV conditions of 60,000 and 120,000 h^{-1}. As shown in Figure 3b, it is noteworthy that even at high GHSV of 120,000 h^{-1}, the catalyst still maintains over 80% NO_x conversion within the temperature range of 225–300 °C. This proves that the excellent space velocity resistance of the Co-Fe (8 h) catalyst.

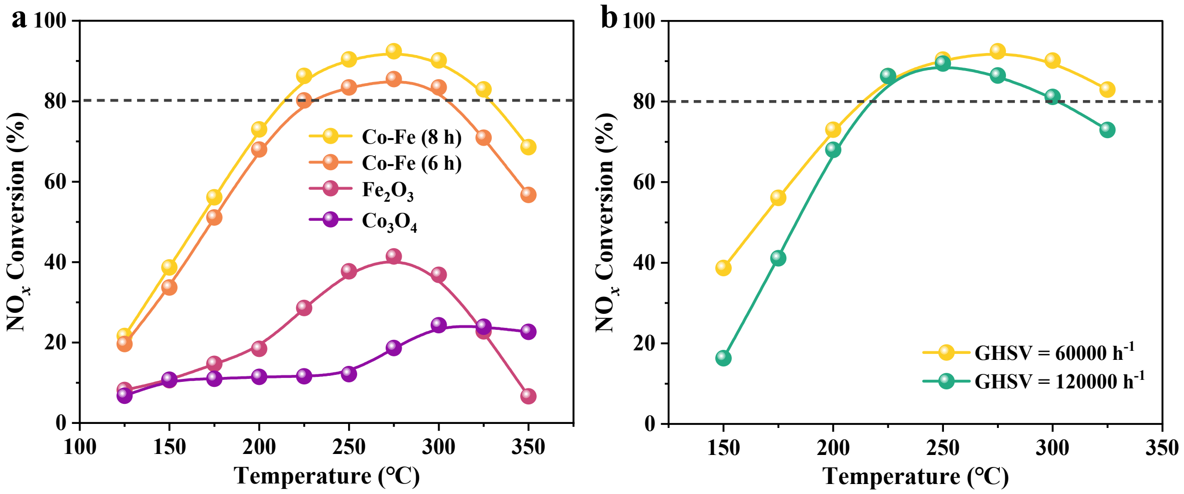

Figure 3. NH_3-SCR performance: (**a**) NO_x conversion over various catalysts; (**b**) NO_x conversion of the Co-Fe (8 h) catalyst under different gas hourly space velocities (GHSV).

3.4. The Behavior of Reactants Adsorption and Activation

NH_3-TPD and NO_x-TPD were employed to probe the adsorption and activation of NH_3 and NO_x, which are critical determinants of NH_3-SCR activity. The resulting profiles are shown in Figure 4.

3.4.1. NH_3 Adsorption Activation Ability

The NH_3 adsorption experiments over the catalysts were studied and the corresponding profiles of catalyst are shown in Figure 4a,b. As is well known, the desorption peak temperature reflects the acid strength of catalyst, while peak area represents the amount of NH_3 adsorbed on acid sites. The desorption peak observed at approximately ~100 °C, 100–200 °C, 200–350 °C and above 350 °C are assigned to physiosorbed NH_3, chemically adsorbed ammonium species on weak acid sites, medium-strong acid sites and strong acid sites, respectively [25,26]. In the NH_3-TPD profile of the Co-Fe (8 h) catalyst (Figure 4a), there are mainly three overlapping desorption peaks are observed at 152 °C, 284 °C and 408 °C, indicating that the acid sites of the catalyst are predominantly weak, medium-strong and strong acid sites [19]. Compared with Co_3O_4, the overall desorption amount of the Co-Fe (8 h) catalyst is enhanced (Figure 4b), indicating that Fe doping results in the formation of an inverse spinel $CoFe_2O_4$ structure, where Fe^{3+} at the tetrahedron and octahedra sites facilitates NH_3 adsorption. In contrast to Fe_2O_3, the Co-Fe (8 h) catalyst shows higher quantities of weak and medium-strong acid sites, together with newly appeared strong acid sites. These improvements can be attributed to the strong acid sites provided by $CoFe_2O_4$, as well as the interaction between Fe_2O_3 and $CoFe_2O_4$ that enhances the overall acid strength.

3.4.2. NO_x Adsorption Activation Ability

As shown in Figure 4c, the NO_x-TPD profiles display several overlapping desorption peaks in the temperature range of 100–550 °C, with the deconvoluted peak integration results provided in Figure 4d. The peaks in the range of 100–250 °C correspond to the decomposition of NO_2, ad-NO_2^- and poorly thermostable monodentate nitrate, while peaks above 250 °C are attributed to highly thermostable nitrate (bridging or/and bidentate) [21,26]. The amount of NO_x desorbed from the Co-Fe (8 h) catalyst is significantly greater than that from the Co_3O_4 and Fe_2O_3 catalysts (Figure 4d). This can be attributed to two factors. First, the inverse spinel $CoFe_2O_4$ structure, where Fe^{3+} ions occupy tetrahedral and octahedral sites, facilitates NO_x adsorption. Second, strong electron interactions reduce the electron cloud density around Co species, thereby enhancing their electrophilicity and promoting the adsorption and stabilization of NO_3^- species.

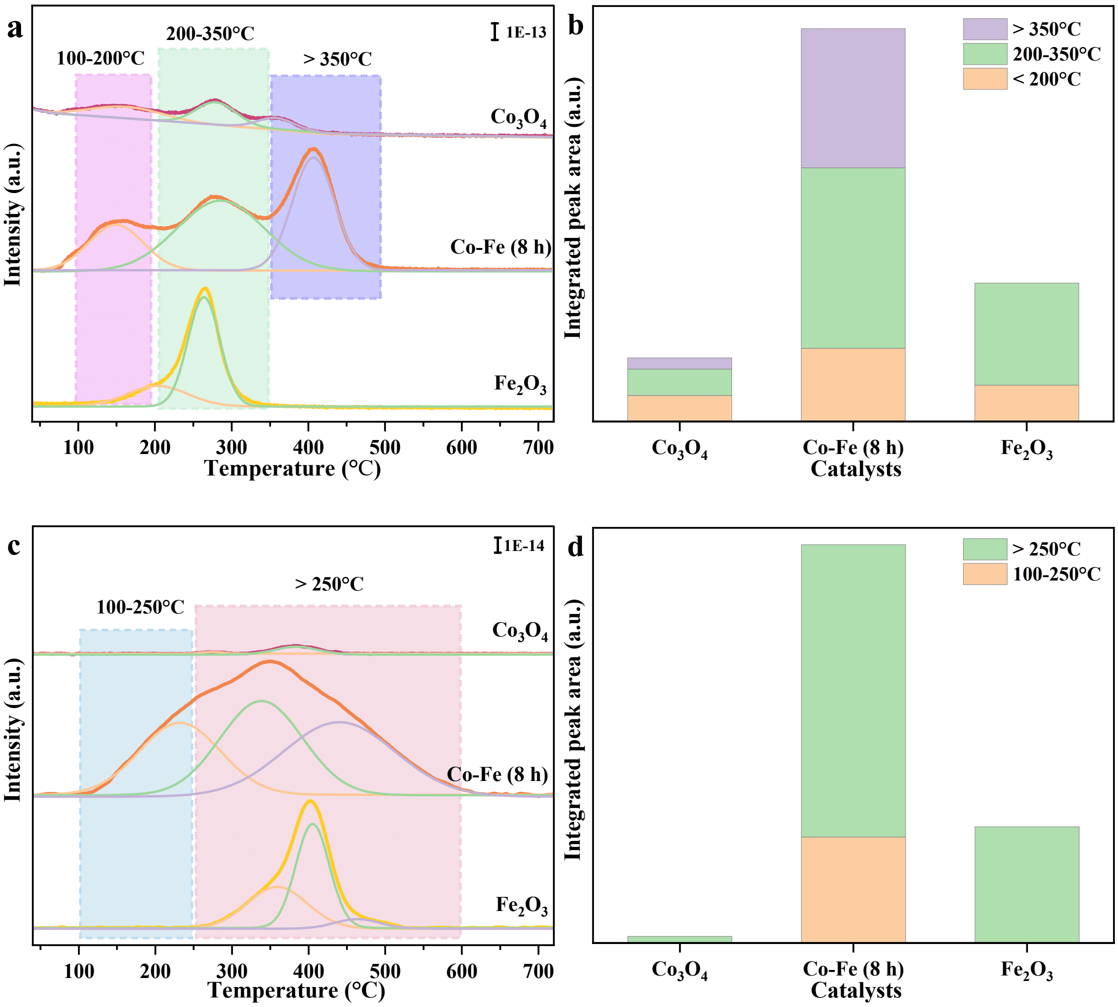

Figure 4. Adsorption and activation capability of various Co-Fe samples: (**a**) NH_3-TPD; (**b**) quantitative analysis of NH_3-TPD profiles; (**c**) NO_x-TPD profiles; (**d**) quantitative analysis of NO_x-TPD profiles.

3.5. Reaction Pathway Determination over Co-Fe (8 h) Catalyst

3.5.1. Identification of NH_3 or NO_x Adsorbed Species and Adsorption Strength

Figure 5a–c display the in situ time-resolved DRIFT spectra of NH_3 adsorption and desorption over Co-Fe (8 h) catalysts at 175 °C. After exposing NH_3 for 30 min (Figure 5a), characteristic bands at 1602, 1207, and 1177 cm^{-1} are assigned to coordinated NH_3 on Lewis acid sites [27,28] The shoulder at 1136 cm^{-1} corresponds to the dehydrogenation of NH_3 to form -NH_2 species [4]. Meanwhile, a weak peak at 1428 cm^{-1} is attributed to NH_4^+ on Brønsted acid sites, indicating that Lewis acid-bound NH_3 is the predominant adsorbed species. Additionally, the band at 1570 cm^{-1} is likely due to bidentate nitrate [29,30], implying partial NH_3 oxidation on the catalyst surface. After purging with He for 30 min, the intensity of NH_3 species decreases significantly. The above-mentioned results manifest that the coordinated NH_3 to the Lewis acid sites is dominated adsorbed species, and the adsorption strength of NH_3 species on the Co-Fe (8 h) catalyst is weak, which favors its migration toward NO_x adsorbed species and subsequent reaction.

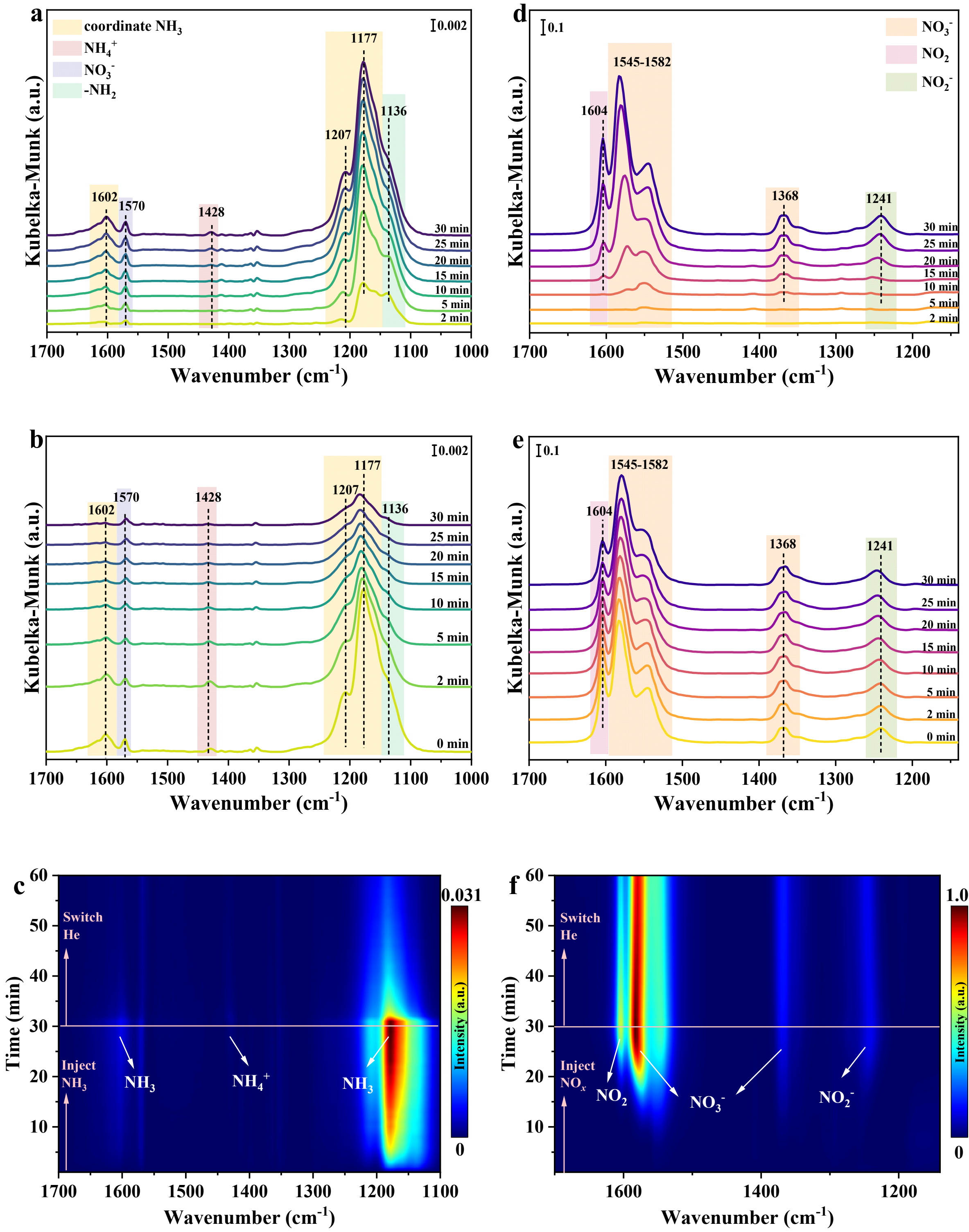

Figure 5. In situ DRIFT spectra of adsorption and desorption of NH_3 (**a**–**c**) and NO + O_2 (**d**–**f**) in 30 min over Co-Fe (8 h) at 175 °C.

To identify the NO_x ad-species, the in situ time-resolved DRIFTS spectra of NO_x adsorption and desorption over Co-Fe (8 h) catalyst were recorded at 175 °C and the corresponding results were shown in Figure 5d−f. When introducing NO + O_2, several distinct bands are detected at 1604 cm^{-1} (gas-NO_2), 1582–1545 cm^{-1} (overlap of bidentate, monodentate nitrate), 1368 cm^{-1} (bidentate nitrate), and 1241 cm^{-1} (nitrite) [31−34]. Noticeably, the adsorbed nitrate and gas-NO_2 were the primary species on Co-Fe (8 h) catalyst. After NO_x was saturated then purged with He for 30 min, the intensity of nitrite and nitrate ad-adsorbed species exhibited only a slight decrease, indicating that the nitrate species is very strongly bounded to the adsorption sites. In contrast, the band assigned to NO_2 shows a significant reduction in intensity upon He purging.

3.5.2. The Reactivity of Pre-Adsorbed NH_3 or NO_x

The reaction between pre-adsorbed NH_3 and NO_x was first recorded at 175 °C. As shown in Figure 6a, the Co-Fe (8 h) catalyst was first treated with NH_3/He for 30 min followed by He purged for 30 min at 175 °C, then the NO + O_2/He was introduced into the IR cell. When NO + O_2 was introduced to the pre-adsorbed catalyst, the bands involving coordinated NH_3 almost disappeared completely within 1 min and the bands which ascribed to NO_x ad-species appeared in succession. With further treatment with NO + O_2, the NO_x ad-species covered catalyst surfaces immediately and dominant with the intensity gradually strengthened. These further evidences that the adsorption capacity of NO_x was much stronger than NH_3 over Co-Fe (8 h) catalyst, which was consistent with the characterization results of NH_3-TPD and NO_x-TPD.

The reaction between pre-adsorbed NO_x and NH_3 over Co-Fe (8 h) catalyst was also recorded at 175 °C. As shown in Figure 6b, the Co-Fe (8 h) catalyst was first treated with NO + O_2/He for 30 min followed by purging He for 30 min at 175 °C, then the NH_3/He was introduced into the IR cell. Upon the introduction of NH_3 into the pre-adsorbed catalyst, the intensity of the band at 1603 cm^{-1} decreases rapidly within 2 min and subsequently stabilized. This is likely attributed to the complete consumption of NO_2 via reaction with adsorbed NH_3, followed by the formation of NH_3 coordinated to Lewis acid sites. The peak assigned to nitrates exhibits a gradual decrease in intensity within 60 min, indicating that the adsorbed NH_3 species can migrate to the nitrate adsorption sites and react via the Langmuir-Hinshelwood (L-H) reaction pathway. Notably, compared with the band of bidentate nitrates, the bands corresponding to monodentate nitrates are rapidly consumed within 10 min, demonstrating that the reactivity of monodentate nitrate adsorption species is significantly superior to that of bidentate nitrates. This implies that the reaction between bidentate nitrate and NH_3 is likely the rate-determining step. Moreover, the band at 1241 cm^{-1} completely disappears within 2 min, while new bands emerge at 1258 and 1280 cm^{-1}, indicating that nitrites react with coordinated NH_3 via the L-H pathway, with NH_3 simultaneously bound to Lewis acid sites.

3.5.3. The NH_3 + NO + O_2 and OFF-ON Experiment of Co-Fe (8 h) Catalyst

To further identify the coexisting species and produced intermediate species during adsorption and reaction, the experiment of NH_3 + NO + O_2 and OFF-ON over Co-Fe (8 h) catalyst was tested at 175 °C to identify the restricting factor of NH_3-SCR reaction. Firstly, treating Co-Fe (8 h) catalyst with the flow of NH_3 + NO + O_2 for 30 min, followed by switching off NO + O_2 for 30 min and then reintroducing NO + O_2 for 30 min. As shown in Figure 6c, upon introduction of NH_3 + NO + O_2, bands at 1603, 1559, 1354, 1209 and 1172 cm^{-1} appear on the catalyst surface within 2 min and intensity of these bands enhancing with the time increasing. The band at 1603 cm^{-1} could be ascribed to overlap of the peaks attributed to gas-NO_2/coordinated NH_3, while the band at 1559 cm^{-1} could be ascribed to bidentate nitrate, respectively. The band at 1354 cm^{-1} may be attributed to the overlap of the peaks of bidentate nitrates and coordinated NH_3. The bands at 1207 and 1172 cm^{-1} are characteristic of coordinated NH_3 species. Compared with the spectrum after 30 min of NO_x adsorption, only an adsorption peaks assigned to bidentate nitrate was detected at 1559 cm^{-1} following the co-adsorption of NH_3 + NO + O_2. This further confirms that monodentate nitrates are more reactive than bidentate nitrate, reacting too quickly with NH_3 species therefore not be undetected on the surface. Therefore, the reaction step between bidentate nitrates and adsorbed NH_3 serves as the rate-determining step.

Subsequently, as shown in Figure 6d, when turned off NO + O_2, the intensity of 1603, 1559 and 1354 cm^{-1} obvious decreased and diminished within 2 min, which further evidence that the adsorbed monodentate nitrate and NO_2 can react with coordinated NH_3 followed L-H mechanism as proved in the reaction between NH_3 and NO_x mentioned above. 10 min after the NO + O_2 flow was stopped, the bands at 1209 and 1172 cm^{-1} continued to strengthen, which was attributed to the formation of NH_3 coordinated to Lewis acid sites. Concurrently, the bands at 1603, 1559, and 1354 cm^{-1} not only reappeared but also steadily intensified. The reason for this phenomenon is the appearance of coordinated NH_3 and NH_2 at 1603 and 1354 cm^{-1}. The increase at 1559 cm^{-1} is attributed to the oxidation of NH_3, resulting in the formation of bidentate nitrates. When NH_3 + NO + O_2 were co-adsorbed, the species attributed to gas-NO_2/NO_2^- were consumed by NH_3. Upon shutting off NO + O_2, these sites adsorbed NH_3 species. Then, when switched on NO + O_2 again, the intensities of all bands decreased due to the reaction between NH_3 and gas-NO_2/NO_2^- ad-species.

Based on the comprehensive characterization and in situ DRIFTS results mentioned above, a complete structure-activity relationship and reaction pathway are schematically illustrated in Figure 6e. The spherical architecture of the Co-Fe (8 h) catalyst provides an intimate Fe_2O_3-$CoFe_2O_4$ interface, where electron transfer from Fe_2O_3 to $CoFe_2O_4$ occurs (evidenced by XPS and H_2-TPR) reduces the electron cloud density of Co species, rendering them more electrophilic and thereby facilitating the adsorption and stabilization of electron-rich NO_3^- species (NO_x-TPD). Meanwhile, the inverse spinel structure of $CoFe_2O_4$, with Fe^{3+} occupying both tetrahedral and octahedral sites, provides abundant Lewis acid sites for NH_3 coordination. Upon co-feeding of reactants, coordinated NH_3 migrates toward the adsorbed nitrate species and reacts via the Langmuir-Hinshelwood pathway. Monodentate nitrates are rapidly consumed due to their high reactivity, whereas the reaction between bidentate nitrates and adsorbed NH_3 proceeds more slowly and is thus identified as the rate-determining step.

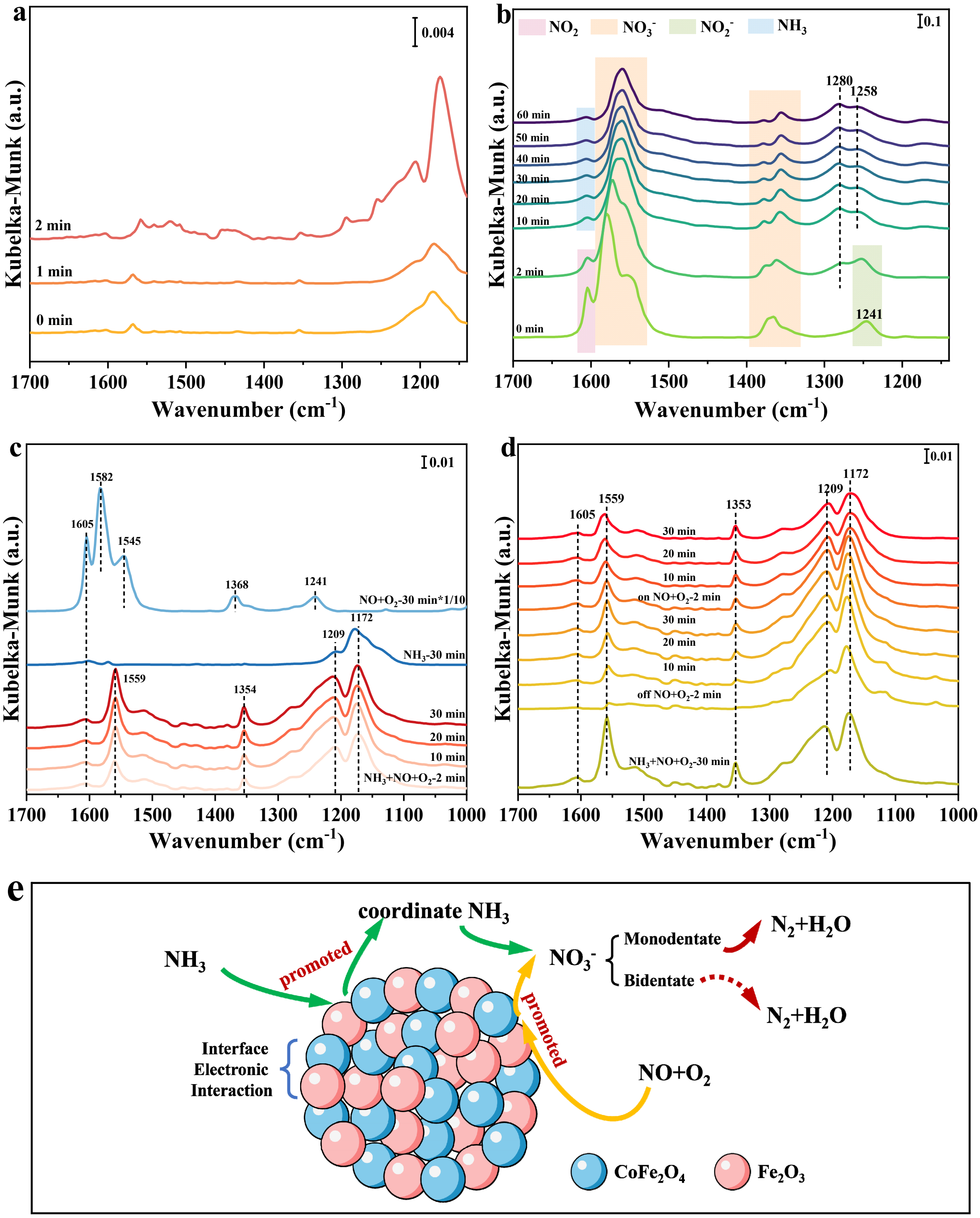

Figure 6. Reaction mechanism: Time-resolved difference in situ DRIFT spectra of (**a**) reaction between NO_x and pre-adsorbed NH_3; (**b**) reaction between NH_3 and pre-adsorbed NO_x; (**c**) adsorption of NH_3 + NO + O_2; (**d**) NO + O_2 off-on over Co-Fe (8 h) catalyst at 175 °C. (**e**) Schematic diagram of reaction mechanism.

4. Conclusions

In this work, a spherical $CoFe_2O_4$-based inverse spinel catalyst was successfully synthesized via the hydrothermal method. The synergistic effect between the $CoFe_2O_4$ inverse spinel and Fe_2O_3 significantly enhanced the reaction activity of the Fe_2O_3-$CoFe_2O_4$ composite catalyst, achieving ≥80% NO_x conversion within the temperature window of 225–325 °C. This is primarily attributed to the strong electronic interaction formed between the two components, which further optimized the redox properties, surface acidity, and adsorption capacity of the catalyst. Such interaction promotes the adsorption and stabilization of NO_3^- species, which then react with NH_3 coordinated to Lewis acid sites following the L-H pathway.

Author Contributions

B.X.: investigation, conceptualization, methodology, visualization, data curation, writing—original draft preparation; T.Z.: investigation, data curation, validation, visualization; H.W.: validation, supervision, writing—reviewing and editing; Z.Q.: supervision, writing—reviewing and editing. All authors have read and agreed to the published version of the manuscript.

Funding

This work was financially supported by the National Natural Science Foundation of China (No. 22476016) and the Fundamental Research Funds for the Central Universities (No. DUT25LAB103). The authors acknowledge the assistance of DUT Instrumental Analysis Center and the assistance of Dr. Xiao Jiang for the technical support in XPS test.

Institutional Review Board Statement

Not applicable.

Informed Consent Statement

Not applicable.

Data Availability Statement

The data that support the findings of this study are available from the corresponding author upon reasonable request.

Conflicts of Interest

The authors declare no competing financial interest.

Use of AI and AI-Assisted Technologies

No AI tools were utilized for this paper.

References

1. Jiang, F.; Li, Z.; Wang, F.; et al. In-depth exploration of NH_3-SCR catalyst improvement research: Sulfur resistance, catalytic activity, and hydrothermal stability. *J. Environ. Chem. Eng.* **2025**, *13*, 119142. https://doi.org/10.1016/j.jece.2025.119142.
2. Leverett, J.; Lie, W.H.; Khan, M.H.A.; et al. Navigating the challenges of global NOx emissions throughout the energy transition: State of play and outlook. *Sustain. Energy Fuels* **2025**, *9*, 3780–3790. https://doi.org/10.1039/d4se01806k.
3. Liu, G.; Sun, H.; Wang, H.; et al. Rational tuning towards B-sites (B = Mn, Co, Al) on CoB_2O_4 binary oxide for efficient selective catalytic oxidation of ammonia. *Chem. Eng. J.* **2023**, *453*, 139941. https://doi.org/10.1016/j.cej.2022.139941.
4. Wang, C.; Yang, S.; Chang, H.; et al. Structural effects of iron spinel oxides doped with Mn, Co, Ni and Zn on selective catalytic reduction of NO with NH_3. *J. Mol. Catal. A Chem.* **2013**, *376*, 13–21. https://doi.org/10.1016/j.molcata.2013.04.008.
5. Xiong, P.; Yang, F.; Ding, Z.; et al. Preparation and electrocatalytic properties of spinel $Co_xFe_{3-x}O_4$ nanoparticles. *Int. J. Hydrog. Energy* **2020**, *45*, 13841–13847. https://doi.org/10.1016/j.ijhydene.2020.03.098.
6. Qin, H.; He, Y.; Xu, P.; et al. Spinel ferrites (MFe_2O_4): Synthesis, improvement and catalytic application in environment and energy field. *Adv. Colloid Interface Sci.* **2021**, *294*, 102486. https://doi.org/10.1016/j.cis.2021.102486.
7. Wang, H.; Hu, Q.; Qiu, J.; et al. Research progress of spinel $CoFe_2O_4$ as an electrocatalyst for the oxygen evolution reaction. *Catal. Sci. Technol.* **2023**, *13*, 6102–6125. https://doi.org/10.1039/d3cy01013a.
8. Kadam, R.A.; Madake, S.B.; Yewale, M.A.; et al. Hierarchical flower-like zinc ferrite photoanode for enhanced photoelectrocatalytic water splitting effect of ammonium fluoride-assisted morphological control. *Solid State Sci.* **2025**, *170*, 108115. https://doi.org/10.1016/j.solidstatesciences.2025.108115.

9. Lazaar, K.; Litaiem, Y.; Farhani, I.; et al. Urchin-like $NiCo_2O_4$ microspheres: An experimental and theoretical study for high-capacity supercapacitors and efficient photocatalysis. *Electrochim. Acta* **2026**, *549*, 148089. https://doi.org/10.1016/j.electacta.2025.148089.
10. Arzuza, L.C.C.; Firmino, H.C.T.; Huaman, N.R.C.; et al. Cobalt ferrite nanofibers for water splitting: Integrating eco-friendly synthesis, calcination control, magnetism and electrocatalytic efficiency. *J. Alloys Compd.* **2025**, *1048*, 185177. https://doi.org/10.1016/j.jallcom.2025.185177.
11. Zheng, F.; Lu, J.; Xu, Q.; et al. ZIF-derived spinel $CoMn_2O_4$ with hierarchically porous architecture and optimized surface chemistry for efficient low-temperature fast NH_3-SCR. *J. Energy Inst.* **2025**, *123*, 102339. https://doi.org/10.1016/j.joei.2025.102339.
12. Hou, S.; Fang, D.; Sheng, F.; et al. Design and regulation of acidic and redox sites in Mn-based spinel for low temperature selective catalytic reduction of NO with NH_3. *Sep. Purif. Technol.* **2025**, *369*, 133054. https://doi.org/10.1016/j.seppur.2025.133054.
13. Zhao, L.; Yang, Y.; Liu, J. Insight into the reaction mechanism of NH_3-SCR and chlorobenzene oxidation over Mn-based spinel catalysts. *J. Hazard. Mater.* **2025**, *492*, 138113. https://doi.org/10.1016/j.jhazmat.2025.138113.
14. Fan, Z.; Fang, W.; Zhang, Z.; et al. Highly active rod-like Co_3O_4 catalyst for the formaldehyde oxidation reaction. *Catal. Commun.* **2018**, *103*, 10–14. https://doi.org/10.1016/j.catcom.2017.09.003.
15. Long, Y.; Zhu, X.; Gao, C.; et al. Modulation of Co spin state at Co_3O_4 crystalline-amorphous interfaces for CO oxidation and N2O decomposition. *Nat. Commun.* **2025**, *16*, 1048. https://doi.org/10.1038/s41467-025-56487-5.
16. Glisenti, M.M.N.a.A. Study of Surface Reactivity of Cobalt Oxides: Interaction with Methanol. *Chem. Mater.* **2002**, *14*, 3090–3099.
17. Saddeler, S.; Hagemann, U.; Bendt, G.; et al. Core-shell Co_3O_4@CoO Nanoparticles for Enhanced OER Activity. *ChemCatChem* **2024**, *16*, e202301327. https://doi.org/10.1002/cctc.202301327.
18. Liu, Z.; Su, H.; Chen, B.; et al. Activity enhancement of WO_3 modified Fe_2O_3 catalyst for the selective catalytic reduction of NO by NH3. *Chem. Eng. J.* **2016**, *299*, 255–262. https://doi.org/10.1016/j.cej.2016.04.100.
19. Wang, H.; Qu, Z.; Dong, S.; et al. Mechanistic Investigation into the Effect of Sulfuration on the FeW Catalysts for the Selective Catalytic Reduction of NO_x with NH_3. *ACS Appl. Mater. Interfaces* **2017**, *9*, 7017–7028. https://doi.org/10.1021/acsami.6b14031.
20. Wang, H.; Qu, Z.; Xie, H.; et al. Insight into the mesoporous $Fe_xCe_{1-x}O_2-\delta$ catalysts for selective catalytic reduction of NO with NH_3: Regulable structure and activity. *J. Catal.* **2016**, *338*, 56–67. https://doi.org/10.1016/j.jcat.2016.02.009.
21. Wang, H.; Qu, Z.; Dong, S.; et al. Superior Performance of $Fe_{1-x}W_xO\delta$ for the Selective Catalytic Reduction of NO_x with NH3: Interaction between Fe and W. *Environ. Sci. Technol.* **2016**, *50*, 13511–13519. https://doi.org/10.1021/acs.est.6b03589.
22. Shao, C.; Liu, X.; Meng, D.; et al. Catalytic performance of Co–Fe mixed oxide for NH_3-SCR reaction and the promotional role of cobalt. *RSC Adv.* **2016**, *6*, 66169–66179. https://doi.org/10.1039/c6ra12025c.
23. Zhang, T.; Zhang, Y.; Ning, P.; et al. The property tuning of NH_3-SCR over iron-tungsten catalyst: Role of calcination temperature on surface defect and acidity. *Appl. Surf. Sci.* **2021**, *538*, 147999. https://doi.org/10.1016/j.apsusc.2020.147999.
24. Chen, Z.; Wang, S.; Ding, Y.; et al. Pd catalysts supported on Co_3O_4 with the specified morphologies in CO and CH_4 oxidation. *Appl. Catal. A: Gen.* **2017**, *532*, 95–104. https://doi.org/10.1016/j.apcata.2016.12.021.
25. Chen, R.; Fang, X.; Li, J.; et al. Mechanistic investigation of the enhanced SO_2 resistance of Co-modified MnOx catalyst for the selective catalytic reduction of NOx by NH3. *Chem. Eng. J.* **2023**, *452*, 139207. https://doi.org/10.1016/j.cej.2022.139207.
26. Wang, H.; Ning, P.; Zhang, Y.; et al. Highly efficient WO_3-FeO catalysts synthesized using a novel solvent-free method for NH3-SCR. *J. Hazard. Mater.* **2020**, *388*, 121812. https://doi.org/10.1016/j.jhazmat.2019.121812.
27. Yu, Y.; Tan, W.; An, D.; et al. Activity enhancement of WO_3 modified FeTiO catalysts for the selective catalytic reduction of NO by NH3. *Catal. Today* **2021**, *375*, 614–622. https://doi.org/10.1016/j.cattod.2019.12.025.
28. Liu, L.; Zhou, Y.; Liu, T.; et al. Highly efficient MnCe/Ti catalyst for NH_3-SCR of NO from sintering flue gas at low temperature: CO tolerance and reaction mechanism assessed by in situ DRIFTS. *Mol. Catal.* **2024**, *553*, 113743. https://doi.org/10.1016/j.mcat.2023.113743.
29. Zhang, T.; Shi, T.; Wang, Y.; et al. Orchestrating dual adsorption sites and unravelling Ce-Mn interaction and reaction mechanisms for efficient NH_3-SCR. *J. Catal.* **2024**, *429*, 115260. https://doi.org/10.1016/j.jcat.2023.115260.
30. Dong, S.; Wang, H.; Zhu, T.; et al. High-performance Fe-Cu composite oxide for selective catalytic reduction of NOx with NH3: Driving of Cu on α-Fe_2O_3. *J. Environ. Chem. Eng.* **2022**, *10*, 108481. https://doi.org/10.1016/j.jece.2022.108481.
31. Wang, H.; Qu, Z.; Dong, S.; et al. Mechanism study of FeW mixed oxides to the selective catalytic reduction of NO with NH_3: In situ DRIFTS and MS. *Catal. Today* **2018**, *307*, 35–40. https://doi.org/10.1016/j.cattod.2017.05.071.
32. Shu, Y.; Sun, H.; Quan, X.; et al. Enhancement of Catalytic Activity Over the Iron-Modified Ce/TiO_2 Catalyst for Selective Catalytic Reduction of NO_x with Ammonia. *J. Phys. Chem. C* **2012**, *116*, 25319–25327. https://doi.org/10.1021/jp307038q.

33. Qi, G.; Yang, R.T.; Chang, R. MnO -CeO_2 mixed oxides prepared by co-precipitation for selective catalytic reduction of NO with NH_3 at low temperatures. *Appl. Catal. B Environ.* **2004**, *51*, 93–106. https://doi.org/10.1016/j.apcatb.2004.01.023.
34. Guo, K.; Zhu, Y.; Yan, Z.; et al. The dual effects of ammonium bisulfate on the selective catalytic reduction of NO with NH3 over Fe_2O_3-WO_3 catalyst confined in MCM-41. *Chem. Eng. J.* **2020**, *389*, 124271. https://doi.org/10.1016/j.cej.2020.124271.